

Phase-field lattice Boltzmann model with singular mobility for quasi-incompressible two-phase flows

Jin Bao¹ and Zhaoli Guo^{2,*}

¹State Key Laboratory of Coal Combustion, School of Energy and Power Engineering, Huazhong University of Science and Technology, Wuhan 430074, China

²Institute of Interdisciplinary Research for Mathematics and Applied Science, Huazhong University of Science and Technology, Wuhan 430074, China

 (Received 5 October 2023; revised 27 December 2023; accepted 5 January 2024; published 15 February 2024)

In this paper, a lattice Boltzmann for quasi-incompressible two-phase flows is proposed based on the Cahn-Hilliard phase-field theory, which can be viewed as an improved model of a previous one [Yang and Guo, *Phys. Rev. E* **93**, 043303 (2016)]. The model is composed of two LBE's, one for the Cahn-Hilliard equation (CHE) with a singular mobility, and the other for the quasi-incompressible Navier-Stokes equations (qINSE). Particularly, the LBE for the CHE uses an equilibrium distribution function containing a free parameter associated with the gradient of chemical potential, such that the variable (and even zero) mobility can be handled. In addition, the LBE for the qINSE uses an equilibrium distribution function containing another free parameter associated with the local shear rate, such that the large viscosity ratio problems can be handled. Several tests are first carried out to test the capability of the proposed LBE for the CHE in capturing phase interface, and the results demonstrate that the proposed model outperforms the original LBE model in terms of accuracy and stability. Furthermore, by coupling the hydrodynamic equations, the tests of double-stationary droplets and droplets falling problems indicate that the proposed model can reduce numerical dissipation and produce physically acceptable results at large time scales. The results of droplets falling and phase separation of binary fluid problems show that the present model can handle two-phase flows with large viscosity ratio up to the magnitude of 10^4 .

DOI: [10.1103/PhysRevE.109.025302](https://doi.org/10.1103/PhysRevE.109.025302)

I. INTRODUCTION

It is still a challenging task in modeling and simulating two-phase flows due to the complex interfacial dynamics that occur across large time and spatial scales, although numerous numerical methods [1–6] have been developed. In recent years, mesoscopic methods based on kinetic theory have been developed as a highly promising tool for simulating two-phase flows. Such methods provide a bridge between microscopic intermolecular interactions and macroscopic two-phase dynamics. In particular, the lattice Boltzmann equation (LBE) method, which mimics intermolecular interactions in a concise and direct way at the mesoscopic scale, has achieved significant advances in modeling two-phase flows [7,8].

A number of two-phase LBE models have been developed from different treatments of the microscopic interactions among fluids at the mesoscopic scale [9–15]. For the color-gradient model [9,10], the different phases were represented by the red and blue particle distribution functions, and the interaction between different phases was realized by the color gradient. For the pseudopotential model [11,12], a pseudopotential function was used to model the nonlocal forces between fluid particles, allowing for the simulation of surface tension and wettability effects. The free-energy model [13,14] used a free-energy density function to account for fluid-fluid

and fluid-solid interactions. The phase-field model [15,16] can be considered as a variant of the free energy model, employing the Ginzburg-Landau free-energy model [17] to describe the interfacial interaction forces between fluids. Particularly, the LBE models based on phase-field theory [16,18–20] have attracted much attention in recent years due to the solid reliable thermodynamic basis. In phase-field theory, a diffusive interface with finite thickness is assumed between different bulk phases such that physical variables (e.g., density and viscosity) vary smoothly across the interface. The flow dynamics can be described by the Navier-Stokes equations coupled with an equation for a phase-field variable (order parameter). There are two widely used models for the field variable, namely, the Cahn-Hilliard equation (CHE) [21,22] and Allen-Cahn equation (ACE) [23,24]. A phase-field LBE model requires two LBE's, solving the phase-field equation and the Navier-Stokes equations, respectively. It is worth noting that addressing the CHE with the LBE method is not trivial where the diffusion term contains a fourth-order gradient term of the order parameter. In order to overcome this defect, some hybrid methods [25–28] coupling CHE and Navier-Stokes equations have been rapidly developed, which integrate LBM for fluid flow and the finite-difference method (FDM) or finite-volume method (FVM) for interface dynamics. For model consistency and to simplify coupling, numerous LBE models have been developed to correctly recover the CHE and accurately describe the motion of phase interface.

*Corresponding author: zlguo@mail.hust.edu.cn

The first phase-field LBE model for two-phase flows was developed by He *et al.* [15]. Zheng *et al.* [29] introduced a spatial difference term in the LBE for the phase-field variable such that the CHE can be recovered. Inspired by this idea, Zu *et al.* [19] absorbed the spatial difference term into the equilibrium distribution function to further improve numerical stability. Liang *et al.* [16] also proposed a multiple-relaxation-time LBE model for CHE where a source term with time derivative was integrated into the evolution equation. In recent work, Zhang *et al.* [30] proposed a high-order LBE model for the CHE through a fourth-order Chapman-Enskog expansion to improve the accuracy and stability in capturing phase interface. It is noted that most of the available phase-field LBE models assume the fluid is incompressible everywhere in the flow domain, which is inconsistent with mass conservation [31]. In order to overcome this defect, Yang *et al.* [32] developed a LBE model based on the quasi-incompressible phase-field theory [31] in which the mass was conserved locally.

In the standard Cahn-Hilliard model, the interfacial dynamics are driven by a force proportional to the gradient of the chemical potential with a constant mobility [21,22,33]. On the other hand, a modified Cahn-Hilliard model with a variable mobility derived from the friction dynamics [33–35] is believed to be more physical, and this leads to the singular CHE. The discrepancies between the standard and singular CHE's were investigated in Ref. [36], and the results showed that numerical dissipation of the singular CHE can be much reduced. Through simulating spinodal decomposition problem, Langer *et al.* [37] showed that variable mobility was important for late-stage spinodal decomposition at low temperatures. The simulation results of spinodal decomposition were in agreement with the experimental results due to the suppression of bulk mobility by using variable mobility [38]. The tests of bubble rising in multicomponent fluids indicated that singular CHE could effectively reduce dissolutions of bubble to surrounding fluid [39]. Furthermore, by simulating two nonidentical stationary droplets immersed in another fluid [33], it is revealed that the singular CHE can provide better numerical prediction than the standard one.

Although numerous LBE models have been developed to solve the standard CHE, no LBE models have been designed for the singular CHE. The difficulty lies in the fact that the variable mobility may be quite small and even zero in the bulk phases, such that the corresponding standard LBE will be unstable. Moreover, most LBE models suffer from numerical instability in simulating two-phase flows with large viscosity ratios [28,40]. The difficulty is that the relaxation time in LBE is limited by the viscosity. When the viscosity ratio of a two-phase system is large, there is bound to be a larger and smaller value of relaxation time. Smaller relaxation time can cause numerical instability, while larger relaxation times can cause the continuity assumption to fail [41]. Inspired by the lattice kinetic scheme [42], in this work we will propose a LBE model for two-phase flows based on the coupled quasi-incompressible Navier-Stokes and singular Cahn-Hilliard equations. Particularly, in the LBE for the singular CHE, a free parameter associated with the gradient of chemical potential is incorporated into the equilibrium distribution function, which can be adjusted according

to the variation of mobility. Moreover, in the LBE for the quasi-incompressible Navier-Stokes equations (qINSE), a free parameter associated with the shear stress tensor is introduced into the equilibrium distribution function, such that the large viscosity ratio problems can be handled. Consequently, the relaxation time can be chosen to ensure numerical stability.

The rest of the paper is organized as follows. In Sec. II, the singular Cahn-Hilliard model for two-phase flows is introduced, and the improved phase-field LBE model is constructed in Sec. III. In Sec. IV, a series of numerical tests are conducted to validate the accuracy of the proposed model. Finally, a brief summary is given in Sec. V.

II. SINGULAR CAHN-HILLIARD MODEL FOR TWO-PHASE FLOWS

In the phase-field theory, the free energy of a two-phase isothermal fluid system can be given as

$$F(\phi) = \int_{\Omega} \left[\psi(\phi) + \frac{\kappa}{2} |\nabla \phi|^2 \right] d\Omega, \quad (1)$$

where ϕ is the phase variable (order parameter), $\psi(\phi)$ is the bulk free-energy density, $\kappa |\nabla \phi|^2/2$ is the interfacial free-energy density with κ being a constant related to the surface tension, and Ω is the control volume. A widely used free-energy density model is the double-well one [43,44]

$$\psi(\phi) = \beta(\phi - \phi_l)^2(\phi - \phi_g)^2, \quad (2)$$

where ϕ_l and ϕ_g represent the order parameters of liquid and gas, and in the present work we set $\phi_l = 1$ and $\phi_g = 0$. κ and β are the functions of surface tension σ and interfacial thickness W

$$\kappa = \frac{3\sigma W}{2|\phi_l - \phi_g|^2}, \quad \beta = \frac{12\sigma}{W|\phi_l - \phi_g|^4}. \quad (3)$$

With the free energy of the system, the chemical potential μ_ϕ can be obtained [43,44]:

$$\begin{aligned} \mu_\phi &= \frac{\delta F}{\delta \phi} = \frac{\partial \psi}{\partial \phi} - \kappa \nabla^2 \phi \\ &= 4\beta(\phi - \phi_l)(\phi - \phi_g) \left(\phi - \frac{\phi_l + \phi_g}{2} \right) - \kappa \nabla^2 \phi. \end{aligned} \quad (4)$$

The evolution of the phase variable can be described by the CHE

$$\partial_t \phi + \nabla \cdot (\phi \mathbf{u}) = \nabla \cdot (M_\phi \nabla \mu_\phi), \quad (5)$$

where \mathbf{u} is the fluid velocity, M_ϕ is the mobility, which takes a constant value M_0 in the standard CHE. In the singular CHE, M_ϕ depends on the order parameter [45]

$$M_\phi = \frac{4}{(\phi_l - \phi_g)^2} M_0 |\phi - \phi_l| |\phi - \phi_g|. \quad (6)$$

It is noted that M_ϕ only works in the interfacial region. The expression of M_ϕ ensures that its maximum value is identical to M_0 , which is necessary for a fair comparison. In other words, the effective Peclet number is identical.

To describe the hydrodynamics of the two-phase system, here we adopt the quasi-incompressible phase-field theory [31], in which the flow is governed by the qINSE:

$$\nabla \cdot \mathbf{u} = -\gamma \nabla \cdot (M_\phi \nabla \mu_\phi), \quad (7a)$$

$$\partial_t(\rho \mathbf{u}) + \nabla \cdot (\rho \mathbf{u} \mathbf{u}) = -\nabla p + \nabla \cdot [\rho \nu (\nabla \mathbf{u} + \nabla \mathbf{u}^T)] + \mathbf{F}, \quad (7b)$$

with

$$\gamma = \frac{\rho_l - \rho_g}{\phi_l \rho_g - \phi_g \rho_l}, \quad (8)$$

where p is the fluid pressure, ν is the kinetic viscosity, $\mathbf{F} = -\phi \nabla \mu_\phi + \mathbf{G}$ is the total force with \mathbf{G} being the body force, and ρ_l and ρ_g are the density of liquid and gas, respectively. $\rho = (\phi - \phi_g)(\rho_l - \rho_g)/(\phi_l - \phi_g) + \rho_g$ is the fluid density.

It is noted that the mass conservation equation $\partial_t \rho + \nabla \cdot (\rho \mathbf{u}) = 0$ simplifies to $\nabla \cdot \mathbf{u} = 0$ in the incompressible phase-field model. However, based on Eq. (5) and the relationship between density and phase variable, the mass conservation equation in the phase field model is actually represented by Eq. (7a). It is obvious that the term $\nabla \cdot (M_\phi \nabla \mu_\phi)$ is nonzero in interfacial region. Therefore, the equation $\nabla \cdot \mathbf{u} = 0$ cannot be satisfied as long as $\rho_l \neq \rho_g$. In other words, the mass is not locally conserved in the incompressible phase-field model. However, the mass is conserved locally in quasi-incompressible phase-field model based on Eq. (7a), and the fluid is compressible in the mixing zone of two incompressible fluids.

III. LATTICE BOLTZMANN MODEL

In this section, we design a double-population LBE model consisting of two LBE's, one for the singular CHE and the other for the qINSE. In order to overcome the drawback that the original LBE model proposed in Ref. [32] (denoted by YG-LBE) cannot handle variable mobility and large viscosity ratio problem, the equilibrium distribution functions for the phase field and flow field are redesigned by introducing the free parameters associated with the chemical-potential gradient and the local shear rate, respectively, so that the two-phase flows with variable mobility and large viscosity ratio can be handled.

A. LBE for the singular CHE

We will first introduce the LBE model for singular CHE which can be written as

$$\begin{aligned} & g_i(\mathbf{x} + \mathbf{c}_i \delta_t, t + \delta_t) - g_i(\mathbf{x}, t) \\ &= -\frac{1}{\tau_g} [g_i(\mathbf{x}, t) - g_i^{eq}(\mathbf{x}, t)] + \left(1 - \frac{1}{2\tau_g}\right) \delta_t R_i(\mathbf{x}, t), \end{aligned} \quad (9)$$

where $g_i(\mathbf{x}, t)$ and $g_i^{eq}(\mathbf{x}, t)$ are the particle distribution function and its equilibrium distribution function at position \mathbf{x} and time t , respectively, \mathbf{c}_i 's are the discrete velocities in the direction i , δ_t represents the time step and τ_g is the relaxation time related to mobility. The equilibrium distribution function is modified by introducing a free parameter associated with

the gradient of chemical potential

$$g_i^{eq} = H_i + \omega_i \phi s_i(\mathbf{u}) + \omega_i A \delta_t \alpha \mathbf{c}_i \cdot \nabla \mu_\phi, \quad (10)$$

where ω_i 's are the weight coefficients, A is a free parameter dependent on the variation of mobility, the expressions of H_i and $s_i(\mathbf{u})$ are given by

$$H_i = \begin{cases} \phi - (1 - \omega_0) \alpha \mu_\phi, & i = 0, \\ \omega_i \alpha \mu_\phi, & i \neq 0, \end{cases} \quad (11a)$$

$$s_i(\mathbf{u}) = \left(\frac{\mathbf{c}_i \cdot \mathbf{u}}{c_s^2} + \frac{\mathbf{u} \mathbf{u} : (\mathbf{c}_i \mathbf{c}_i - c_s^2 \mathbf{I})}{2c_s^4} \right), \quad (11b)$$

where c_s is the lattice sound speed, and the parameter α in Eq. (11a) is set to be 1 in the present model, R_i is the forcing term which can be written as

$$R_i = -\frac{\phi}{c_s^2 \rho} (\mathbf{c}_i - \mathbf{u}) \cdot (\nabla p - \mathbf{F}) \omega_i T_i(\mathbf{u}), \quad (12)$$

where $T_i(\mathbf{u}) = 1 + s_i(\mathbf{u})$. The order parameter can be obtained by

$$\phi = \sum_i g_i. \quad (13)$$

It should be noted that modifications to the equilibrium distribution can also be incorporated into the forcing term with $R'_i = R_i + \frac{2}{(2\tau_g - 1)\delta_t} \omega_i A \delta_t \alpha \mathbf{c}_i \cdot \nabla \mu_\phi$; essentially, they are equivalent.

In the present work, we only consider two-dimensional problems, and the two-dimensional nine-velocity (D2Q9) model is employed, in which the discrete velocities are given by $\mathbf{c}_0 = (0, 0)$, $\mathbf{c}_{i=1-4} = c\{\cos[(i-1)\pi/2], \sin[(i-1)\pi/2]\}$, $\mathbf{c}_{i=5-8} = \sqrt{2}c\{\cos[(2i-1)\pi/4], \sin[(2i-1)\pi/4]\}$, and the corresponding weight coefficients are $\omega_0 = 4/9$, $\omega_{1-4} = 1/9$, $\omega_{5-8} = 1/36$. The lattice sound speed is defined by $c_s = c/\sqrt{3}$, where $c = \delta_x/\delta_t$ with δ_x being the lattice space. For simplicity, the lattice units are used, i.e., $\delta_x = \delta_t = 1$. The gradient and Laplace operators are discretized using the second-order isotropic schemes [16,46,47]

$$\nabla \phi(\mathbf{x}, t) = \sum_i \frac{\omega_i \mathbf{c}_i \phi(\mathbf{x} + \mathbf{c}_i \delta_t, t)}{c_s^2 \delta_t}, \quad (14a)$$

$$\nabla^2 \phi(\mathbf{x}, t) = \sum_i \frac{2\omega_i [\phi(\mathbf{x} + \mathbf{c}_i \delta_t, t) - \phi(\mathbf{x}, t)]}{c_s^2 \delta_t^2}. \quad (14b)$$

The target CHE can be correctly recovered via Chapman-Enskog analysis of Eq. (9) (see details in Appendix), and the mobility can be obtained:

$$M_\phi = c_s^2 \alpha \delta_t (\tau_g - \frac{1}{2} - A). \quad (15)$$

Moreover, the gradient of chemical potential can also be obtained by considering the first-order moment of the nonequilibrium part of distribution function

$$\nabla \mu = \frac{\sum_i \mathbf{c}_i (g_i - g_i^{eq(0)}) - \frac{1}{2} \delta_t \frac{\phi}{\rho} \nabla p}{(A - \tau_g) \delta_t c_s^2 + \frac{1}{2} \delta_t \frac{\phi^2}{\rho}}, \quad (16)$$

where $g_i^{eq(0)} = H_i + \omega_i \phi s_i(\mathbf{u})$. It can be shown that the proposed LBE composed of Eqs. (9), (10), and (12) can recover exactly the singular CHE (Appendix).

B. LBE for the qINSE

The LBE with a BGK collision operator for the Navier-Stokes equations is given by [32]

$$\begin{aligned} & f_i(\mathbf{x} + \mathbf{c}_i \delta_t, t + \delta_t) - f_i(\mathbf{x}, t) \\ &= -\frac{1}{\tau_f} [f_i(\mathbf{x}, t) - f_i^{eq}(\mathbf{x}, t)] + \left(1 - \frac{1}{2\tau_f}\right) \delta_t F_i(\mathbf{x}, t), \end{aligned} \quad (17)$$

where $f_i(\mathbf{x}, t)$ is the distribution function for particles at position \mathbf{x} and time t , τ_f is the relaxation time related to the fluid viscosity. The equilibrium distribution function is redefined by introducing a free parameter associated with the local shear rate

$$f_i^{eq} = \omega_i [p + c_s^2 \rho s_i(\mathbf{u})] + \frac{1}{2} \rho \omega_i B \delta_t \mathbf{S} : (\mathbf{c}_i \mathbf{c}_i - c_s^2 \mathbf{I}), \quad (18)$$

where B is a free parameter related to the kinetic viscosity, $\mathbf{S} = \nabla \mathbf{u} + (\nabla \mathbf{u})^T$ is the shear stress tensor, \mathbf{I} is the identity tensor. The discrete forcing term in Eq. (17) is given by [32]

$$\begin{aligned} F_i &= (\mathbf{c}_i - \mathbf{u}) \cdot [\omega_i \mathbf{F} \Gamma_i(\mathbf{u}) + \omega_i s_i(\mathbf{u}) c_s^2 \nabla \rho] \\ &\quad - \omega_i c_s^2 \rho \gamma \nabla \cdot (M_\phi \nabla \mu). \end{aligned} \quad (19)$$

The pressure and velocity of fluid can be obtained by taking the zero-order and first-order moments of the distribution

function

$$p = \sum_i f_i(\mathbf{x}, t) + 0.5 \delta_t c_s^2 [\mathbf{u} \cdot \nabla \rho - \gamma \rho \nabla \cdot (M_\phi \nabla \mu)], \quad (20a)$$

$$\rho c_s^2 \mathbf{u} = \sum_i \mathbf{c}_i f_i(\mathbf{x}, t) + 0.5 \delta_t c_s^2 \mathbf{F}. \quad (20b)$$

Through the Chapman-Enskog analysis, it can be shown that the qINSE [Eq. (7)] can be recovered from the LBE [Eq. (17)], with the kinetic viscosity given by

$$\nu = c_s^2 \delta_t (\tau_f - 0.5 - B). \quad (21)$$

Moreover, the term of shear stress tensor can be calculated from nonequilibrium part of the distribution function

$$\mathbf{S} = \frac{\sum_i \mathbf{c}_i \mathbf{c}_i (f_i - f_i^{e(0)}) + \frac{\delta_t}{2} [c_s^4 \mathbf{u} \cdot \nabla \rho \mathbf{I} + c_s^2 (\mathbf{F}_0 \mathbf{u} + \mathbf{u} \mathbf{F}_0)]}{\rho c_s^4 \delta_t (A - \tau_f)}, \quad (22)$$

where $f_i^{e(0)} = \omega_i [p + c_s^2 \rho s_i(\mathbf{u})]$, and $\mathbf{F}_0 = \mathbf{F} + c_s^2 \nabla \rho$.

Remark I: The proposed model reduces to the YG-LBE by setting $A = B = 0$. Note that the relaxation time is coupled with the mobility. In other words, the mobility cannot be too small or zero in the YG-LBE model. If the idea of singular CHE is introduced into YG-LBE model, where the mobility varies continuously (and even zero), numerical instability will be encountered. In addition, the relaxation time for the flow field in the YG-LBE model is constrained by the viscosity, making it difficult to simulate two-phase flows with large

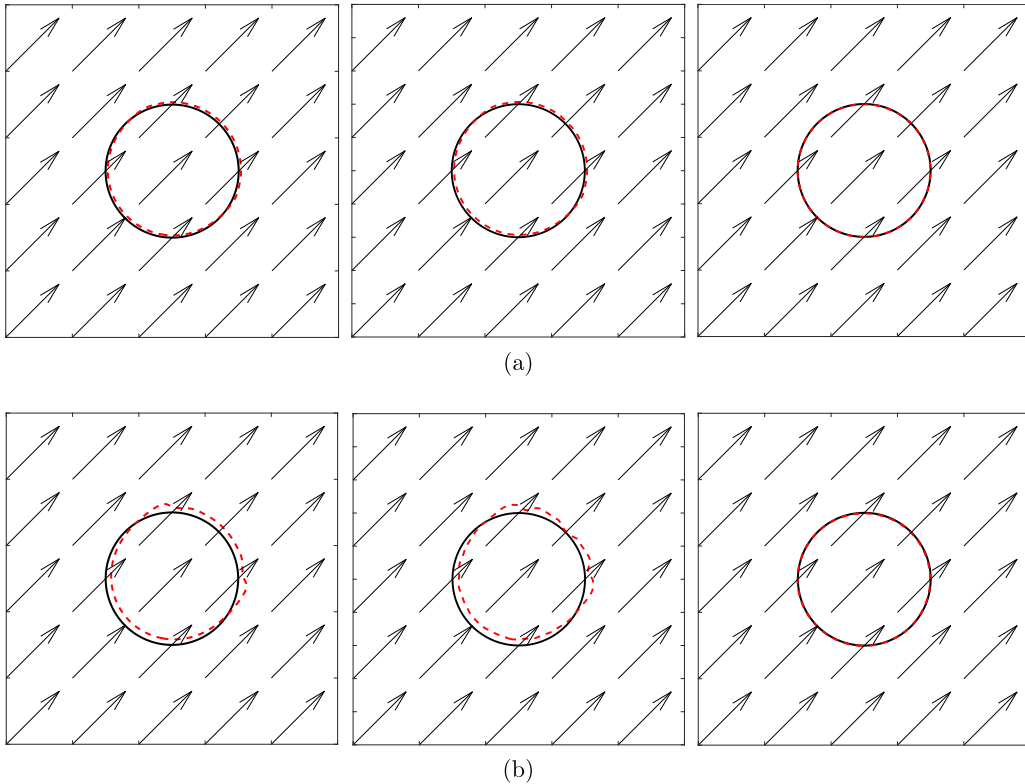


FIG. 1. Comparison of the interface shape after one period and ten periods with the initial shape at $Pe = 2000$ for the droplet diagonal translation test. From left to right, the results predicted by the YG-LBE, SCH-YG-LBE, and the present models. The black solid line denotes $t = 0$, the red dashed line denotes $t = nT$. (a) $n = 1$, (b) $n = 10$.

viscosity ratios. However, by introducing the free parameters, the relaxation time of the proposed model overcomes the limitations of the mobility and fluid viscosity, making it capable of handling two-phase flows with varying mobility and/or large viscosity ratio.

Remark II: In order to avoid the YG-LBE model handling with zero mobility when the so-called singular CHE is introduced, an alternative approach (denoted by SCH-YG-LBE) is to choose a very small mobility ($M_\phi = 1.0 \times 10^{-6}$) for the bulk region, while the mobility in the interfacial region is still obtained by Eq. (6). Due to $\nabla\mu_\phi$ in Eq. (5) being zero in the bulk region, choosing a small value also ensures that the right-hand side of Eq. (5) remains close to 0, thus the diffusion in the bulk phase can be suppressed. However, as described in Remark I, the small mobility implies that the relaxation time is close to 0.5, leading to numerical instability in the LBE model. In the following simulation, we will prove that the SCH-YG-LBE model is numerically unstable.

IV. NUMERICAL TESTS

In this section, several tests are conducted to validate the accuracy and stability of the proposed LBE model. Firstly, several two-dimensional benchmark problems, including the diagonal translation of a circular interface, the Zalesak’s disk rotation, and the single vortex are employed to test the capability of the LBE for the singular CHE in capturing phase interface. A comparison between the proposed model and the YG-LBE will also be made. Then, two-dimensional (2D) dynamic problems, namely, the stationary liquid droplet immersed in gas phase, a droplet falling in a channel and phase separation of binary fluid, are simulated by the present LBE model to examine its performance in simulating two-phase flows. Periodic boundary conditions are applied to the four boundaries in the simulations unless otherwise specified. The dimensionless Peclet number $Pe = (U_0W)/(M_0\beta)$ is adopted, which ensures that the effective Peclet is identical for both standard and singular CHE models. To quantitatively compare the accuracy of interface capture between the proposed model and the YG-LBE model, the L_2 -norm and maximum relative errors are used [30]:

$$\|E(\phi)\|_2 = \sqrt{\frac{\sum_x |\phi(\mathbf{x}, nT) - \phi(\mathbf{x}, 0)|^2}{\sum_x |\phi(\mathbf{x}, 0)|^2}}, \quad (23a)$$

$$\|E(\phi)\|_{\max} = \frac{\max |\phi(\mathbf{x}, nT) - \phi(\mathbf{x}, 0)|}{|\phi_l - \phi_g|}. \quad (23b)$$

A. Diagonal translation of a circular interface

Firstly, the motion of a circular droplet in a constant velocity field $\mathbf{u} = (U_0, U_0)$ is studied. Initially, a droplet of radius $R = L_0/5$ is placed at the center of the computational domain $L_0 \times L_0$. After one period $T = L_0/U_0$, the droplet returns to its initial position. In the simulations, we set: $Pe = 2000$, $\alpha = 1$, $\sigma = 0.01$, $U_0 = 0.02$, $\rho_l = \rho_g = 1$, $L_0 = 200$, $W = 0.02L_0$. In addition, we take $\tau_g = 0.8$ in the present model, and the value of parameter A can be obtained by Eq. (15).

Figure 1 shows the comparison of the interface shape predicted by the YG-LBE, SCH-YG-LBE, and the present

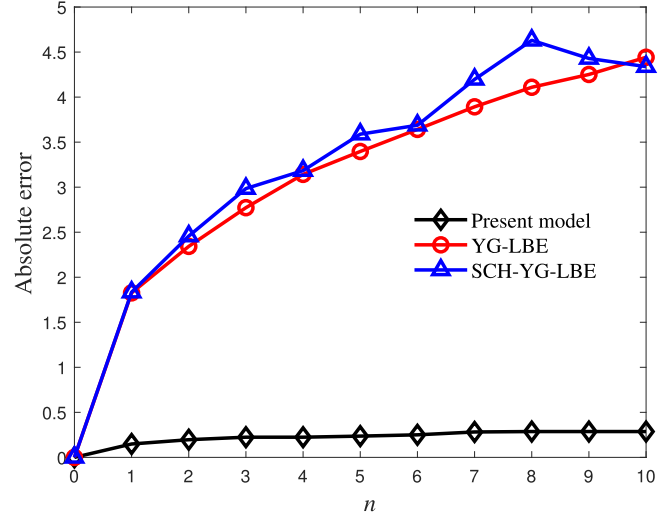


FIG. 2. The absolute error between the theoretical and numerical values of the center of mass.

models after one period and ten periods with the initial shape at $Pe = 2000$. After one period, a slight discrepancy can be observed between the interface predicted by the YG-LBE model and the initial one, which becomes more significant after ten periods. As shown in Fig. 1(b), similar results can also be observed in the SCH-YG-LBE model, which indicates that this approach leads to numerical instability. On the other hand, the results obtained by the present model after one and ten periods are in good agreement with the initial interface. It is noted that the nonalignment of the enforced velocity with the lattice directions does not significantly impact the results due to the sufficient accuracy of the D2Q9 discrete velocity model in simulating two-dimensional fluid flows. Figure 2 further presents the absolute errors between the theoretical and numerical positions of the center of mass at $Pe = 2000$. It can be seen that for the YG-LBE model the absolute error increases gradually with the increase of period, and after ten periods the difference between the numerical results and theoretical values exceeds one interface thickness. This clearly indicates that the YG-LBE model yields incorrect interfacial properties; Similar results have been observed in the SCH-YG-LBE model. However, it exhibits larger errors compared to the YG-LBE model. Consequently, the SCH-YG-LBE model will not be included in further comparisons in this study; while for the present model, the numerical results are close to the theoretical value even after ten periods. We also investigate the relative errors of the two models at different Pe numbers.

TABLE I. Relative errors of the interface after one period with different Pe numbers for the droplet diagonal translation problem.

Pe	$\ E(\phi)\ _2$		$\ E(\phi)\ _{\max}$	
	YG-LBE model	Present model	YG-LBE model	Present model
20	0.0377	0.0064	0.2022	0.0378
200	0.0833	0.0089	0.3715	0.0444
2000	0.1320	0.0096	0.3354	0.0457

TABLE II. Relative errors of the interface after ten periods with different Pe numbers for the droplet diagonal translation problem.

Pe	$\ E(\phi)\ _2$		$\ E(\phi)\ _{\max}$	
	YG-LBE model	Present model	YG-LBE model	Present model
20	0.1477	0.0132	0.6790	0.0842
200	0.2541	0.0237	0.7523	0.0855
2000	0.3535	0.0275	0.6149	0.0840

The relative errors of the phase interface after one and ten periods for the droplet diagonal translation problem with different Pe numbers are given in Tables I and II, respectively. It is clear that both L_2 -norm and maximum relative errors are large after one period for the YG-LBE model, and these errors far exceed the acceptable error range after ten periods. On the other hand, the present model gives satisfactory results after one and ten periods, particularly at high Pe number.

To investigate the effect of Mach number ($Ma = U_0/c_s$) on the numerical results, Fig. 3 shows the interface shapes predicted by the two models after ten periods at different Mach numbers. It can be seen from Fig. 3(a) that with the increase of Mach number, the interface predicted by the YG-LBE model suffers from severe deformation and numerical instability occurs, further increasing Mach number to 0.139 the procedure diverges. However, as shown in Fig. 3(b) for the present model, the predicted interface shape agrees well with the initial shape, with only slight difference at high Mach number. Figure 4 gives the variation of relative error of L_2 -norm with Mach number after ten periods. It can be seen that as the Mach number increases, the relative errors obtained by both models increase, but the error of the present model is much smaller than that of the YG-LBE model. The results for the diagonal translation of circular interface confirm that the present model has the capability of tracking the phase interface with improved accuracy and numerical stability.

B. Zalesak’s disk rotation

The Zalesak’s disk rotation [19,48] is widely used to test the capability of numerical methods in capturing phase interface. Initially, a circular disk with a slot is placed at the center of computational domain with a lattice size of $L_0 \times L_0$.

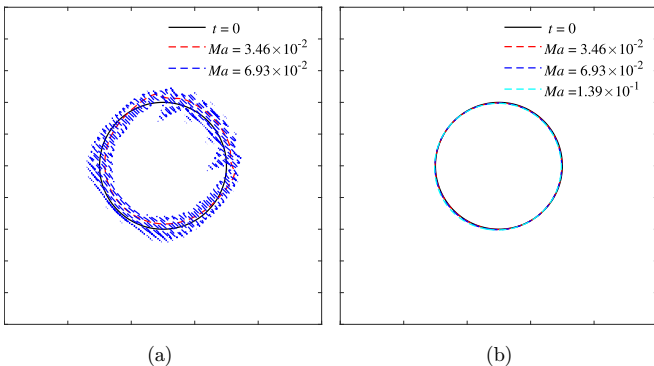


FIG. 3. Interface shapes after ten periods at different Ma number predicted by (a) the YG-LBE model, (b) the present model.

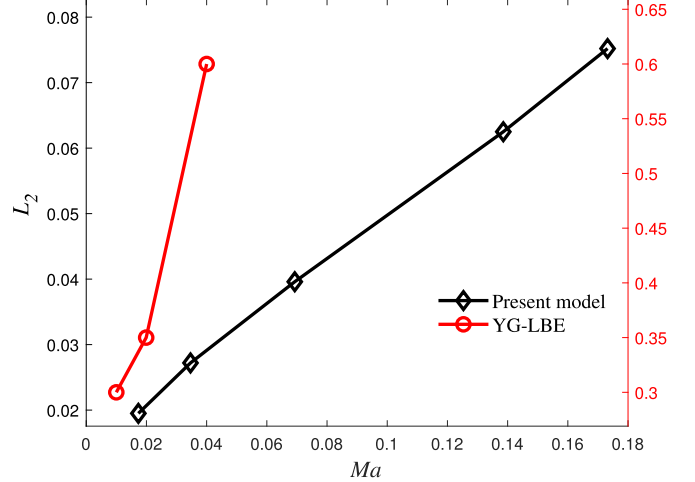


FIG. 4. Relative error of L_2 -norm for the diagonal translation problem at different Ma number after ten periods.

In this problem, the radius of disk and the width of slot are set as $0.4L_0$ and $0.08L_0$, respectively. The rotation of the disk is driven by a flow field with given rotational velocity

$$u = -U_0\pi\left(\frac{y}{L_0} - 0.5\right), \quad v = U_0\pi\left(\frac{x}{L_0} - 0.5\right); \quad (24)$$

with the above settings, the disk will start to rotate and retains its shape during the whole simulation process, and finally returning to its initial position after one period $T = 2L_0/U_0$. In the simulations, we set: $L_0 = 200, U_0 = 0.02, \rho_l = \rho_g = 1, \sigma = 0.01, \alpha = 1, W = 0.02L_0$. In addition, we take $\tau_g = 0.8$ in the present model, and the value of parameter A can be obtained by Eq. (15).

Figure 5 presents the comparison of interface shape with the initial one at different Pe numbers for $t = (2L_0)/U_0$ and $t = (10L_0)/U_0$. It is obvious that the interface predicted by the YG-LBE model produces distinct deformation in the vicinity of the slot after one period, and the deformation is even more significant at $t = (10L_0)/U_0$. On the other hand, the present model still accurately captures the interface at $t = (10L_0)/U_0$, with slight difference at the corners of the slot. This is due to the corners of the slot being initialized as a sharp interface. The L_2 -norm relative errors at $t = (2L_0)/U_0$ and $t = (10L_0)/U_0$ for different Pe numbers are shown in Table III. Compared with the results of YG-LBE model, the present model exhibits smaller errors for each Pe number. To further demonstrate the ability of the present model to capture the interface, the absolute errors between the theoretical

TABLE III. The L_2 -norm relative errors of the interface at $t = (2L_0)/U_0$ and $t = (10L_0)/U_0$ with different Pe numbers for Zalesak’s disk rotation problem.

Pe	$t = (2L_0)/U_0$		$t = (10L_0)/U_0$	
	YG-LBE model	Present model	YG-LBE model	Present model
20	0.0217	0.0159	0.0537	0.0222
200	0.0239	0.0159	0.0529	0.0222
2000	0.0310	0.0159	0.0566	0.0222

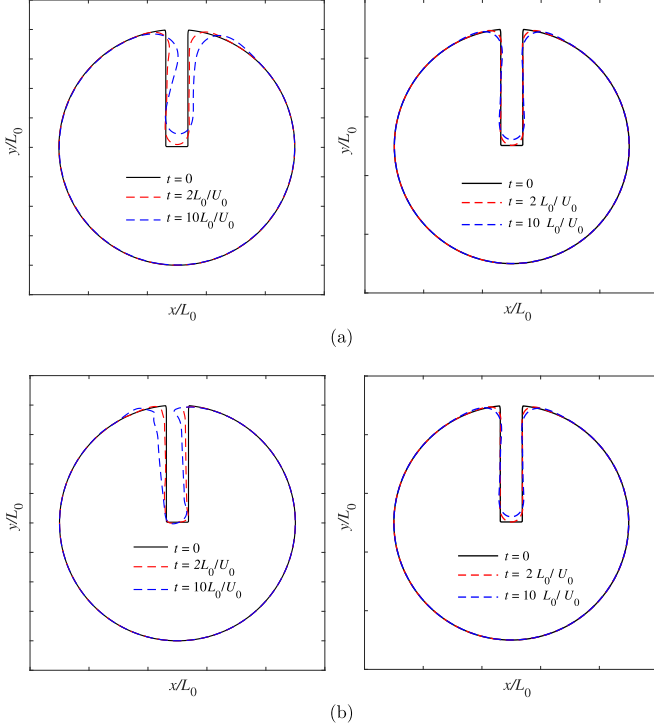


FIG. 5. Comparison of the interface shape at $t = (2L_0)/U_0$ and $t = (10L_0)/U_0$ with initial shape for Zalesak's disk problem at (a) $Pe = 20$ and (b) $Pe = 2000$. From left to right, the results predicted by the YG-LBE model and the present model.

and numerical rotation angles are shown in Table IV. Once again, the present model yields minimal absolute errors for various Pe numbers and periods. Furthermore, the influence of Mach number on the simulation results for the Zalesak's disk rotation problem is analogous to the effect observed in the problem of diagonal translation of a circular interface. Figure 6 shows the distribution of interface shape obtained from the two models with different Mach number at $t = (10L_0)/U_0$. It can be seen from Fig. 6(a) that with the increase of Mach number, the interface predicted by the YG-LBE model suffers from severe numerical instability, and the procedure diverges with increasing Mach number to 0.139; While for the present model [as shown in Fig. 6(b)], the predicted interface shape agrees well with the initial shape for different Mach numbers. The results of the Zalesak's disk rotation confirm again that the present model can capture the interface with improved accuracy.

TABLE IV. The absolute errors between the measured and analytical rotation angles for Zalesak's disk rotation problem.

Pe	$t = (2L_0)/U_0$		$t = (10L_0)/U_0$	
	YG-LBE model	Present model	YG-LBE model	Present model
20	2.59°	0.34°	11.74°	1.77°
200	2.06°	0.30°	7.21°	1.49°
2000	0.98°	0.29°	5.19°	1.46°

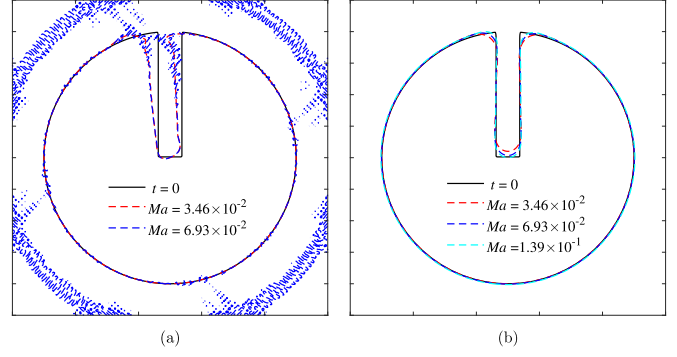


FIG. 6. Interface shapes for different Ma number predicted by (a) the YG-LBE model, (b) the present model at $t = (10L_0)/U_0$.

C. Single vortex

It is worth noting that the aforementioned two tests do not involve interfacial topology changes. In order to further validate the ability of the present model to handle complex interfacial deformation, the single-vortex test is used for the following simulation, where the velocity field is time dependent and stronger nonlinear,

$$\begin{aligned}
 u &= U_0 \sin^2 \frac{\pi x}{L_0} \sin \frac{2\pi y}{L_0} \cos \frac{\pi t}{T}, \\
 v &= -U_0 \sin \frac{2\pi x}{L_0} \sin^2 \frac{\pi y}{L_0} \cos \frac{\pi t}{T},
 \end{aligned} \quad (25)$$

where $T = nL_0/U_0$ is the period with n being a positive integer. In this problem, a circular interface of radius $R = L_0/5$ is placed at $(0.5L_0, 0.75L_0)$ of the computational domain, which has a lattice size of $L_0 \times L_0$. The given velocity field drives the deformation of the circular interface, causing its stretch and then reaches its maximum deformation at $t = T/2$. Subsequently, the interface returns to its initial shape after one period. In the simulations, we set: $L_0 = 200$, $U_0 = 0.04$, $\rho_l = \rho_g = 1$, $\sigma = 0.001$, $\alpha = 1$, $W = 0.01L_0$. In addition, we take $\tau_g = 0.8$ in the present model, and the value of parameter A can be obtained by Eq. (15).

Figure 7 presents the interface shapes predicted by both the YG-LBE and the present models at different time with $Pe = 500$ and $n = 6$. It is obvious that the results predicted by the YG-LBE model produce some undesired diffusion in the vicinity of the interface, while the present model captures the interface with improved stability. To further test the capability of the present model at high Pe number, the interface predicted by the present model for different n values at $Pe = 5000$ is shown in Fig. 8. The numerical predictions are similar to the initial shape for different n values. Table V shows the L_2 -norm and area conservation relative errors predicted by the

TABLE V. Relative errors obtained by the present model for different n values at $Pe = 5000$.

n	$\ E(\phi)\ _2$	$E(\phi)_{\text{area}}^{T/2}$	$E(\phi)_{\text{area}}^T$
2	0.0290	0.0034	0.0020
4	0.0549	0.0006	0.0024
6	0.0820	0.0054	0.0020

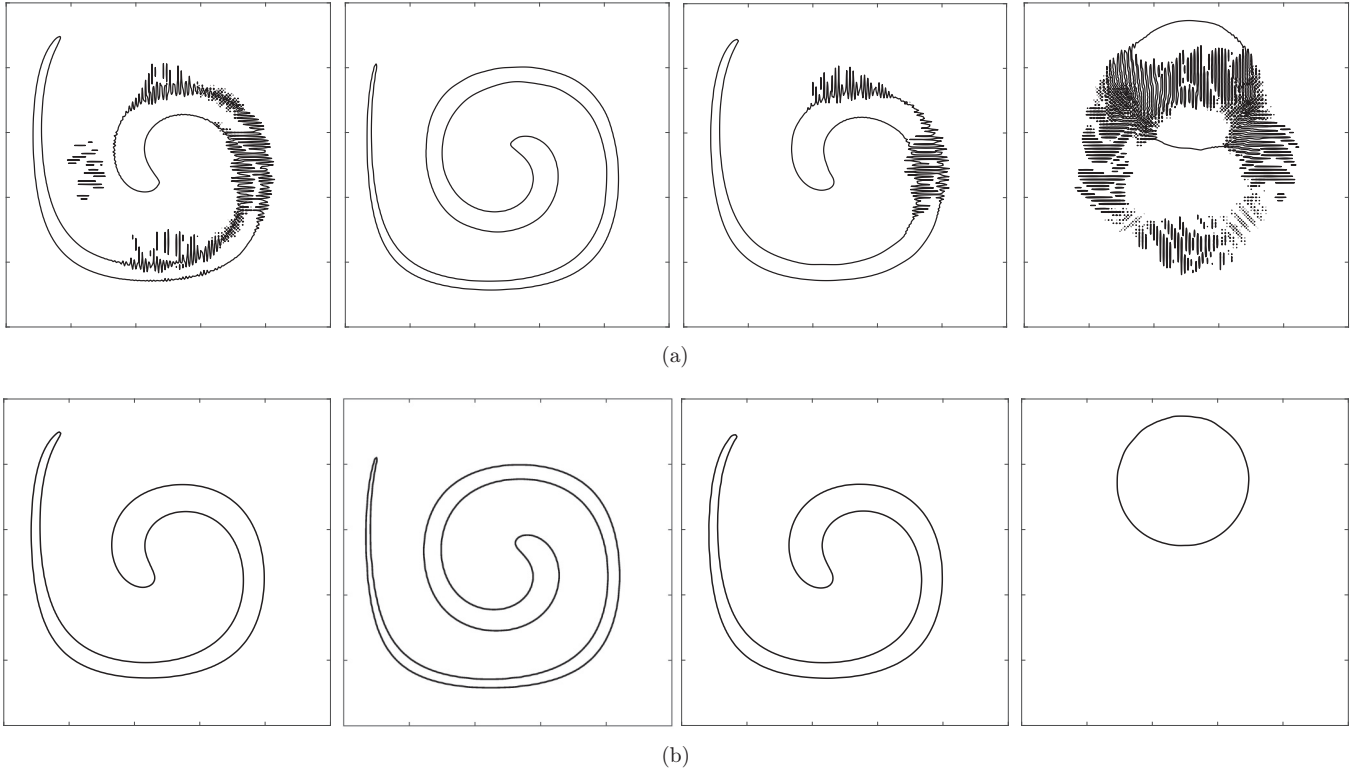


FIG. 7. Results of single-vortex problem at $Pe = 500$ and $n = 6$ for (a) the YG-LBE model (b) the present model. From left to right $T/4, T/2, 3T/4, T$.

present model at $Pe = 5000$. As shown in Table V, the results of relative error for different n values indicate that the good conservation property of the present model can be maintained:

$$E(\phi)_{\text{area}}^T = \frac{\sum_{\phi(x,T)>0.5} 1 - \sum_{\phi(x,0)>0.5} 1}{\sum_{\phi(x,0)>0.5} 1}. \quad (26)$$

D. Two stationary droplets immersed in the gas phase

To further investigate the capacity of the proposed model in simulating two-phase flows, the dynamic behaviors of large and small droplets immersed in the gas phase are investigated using both the YG-LBE and the present models. Initially, two stationary droplets with radius R_1 and R_2 are placed at $(13L_0/30, L_0/2)$ and $(7L_0/10, L_0/2)$ of a

computational domain with the size of $L_0 \times L_0$, respectively. In the simulations, we set: $\rho_l = 5.0, \rho_g = 1.0, \nu_l = 0.1, \nu_g = 0.05, \sigma = 0.001, L_0 = 300, R_1 = L_0/6, R_2 = L_0/30, W = 0.01L_0, M_0 = 0.08, \tau_g = 0.75$, and $B = 0$. In addition, the value of parameter A in the present model can be obtained by Eq. (15). The time is dimensionless by the viscous time $T_v = (\mu_g R_1)/\sigma$, i.e., $T_r = t/T_v$. Figure 9 plots a few snapshots of phase variable at different time predicted by the YG-LBE model. It can be seen that with the increase of time, the volume of small droplet gradually decreases until it disappears completely at $T_r = 3200$. It is noted that the distance between the two droplets is much further than that at which coalescence occurs. This unphysical phenomenon has also been mentioned in previous simulations using the CHE model [33,49]. This result arises from the high-order

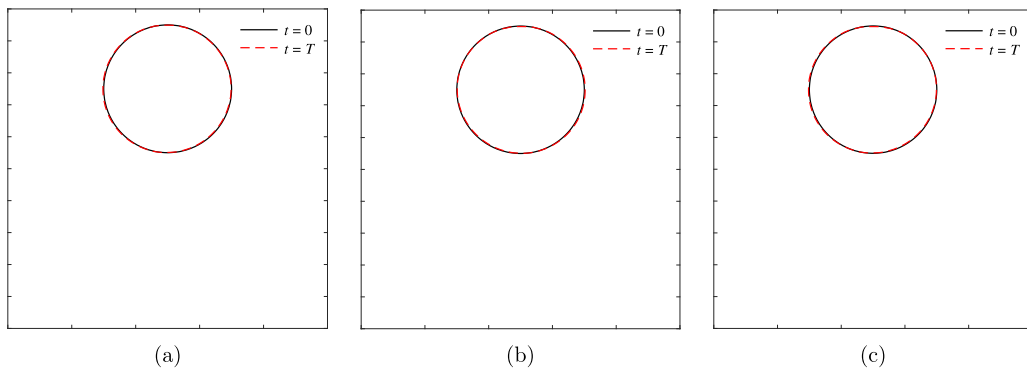


FIG. 8. Interface shapes predicted by the present model at $Pe = 5000$. (a) $n = 2$, (b) $n = 4$, (c) $n = 6$.

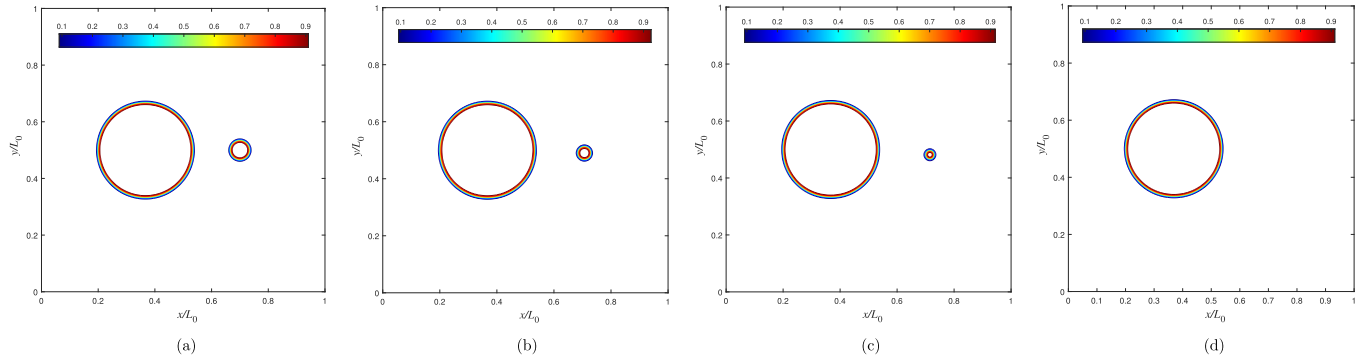


FIG. 9. The snapshots of two static droplets at different time obtained by the YG-LBE model. (a) $T_r = 0$, (b) $T_r = 2000$, (c) $T_r = 2800$, (d) $T_r = 3200$.

dissipation of the diffusion term in the numerical treatment of the CHE. On the other hand, the snapshots of double droplets predicted by the present model at $T_r = 2000$ and $T_r = 3200$ under the same parameter settings are shown in Fig. 10. It is clear that the unphysical phenomenon of the small droplet disappearing is effectively suppressed and the two droplets still maintain their initial positions and sizes. In order to explain the disappearance of small droplet, we compare the distribution of the phase variable and transport flux ($J_x = M_\phi \partial_x \mu$) across the droplets center obtained by the two models at $T_r = 2800$, and the comparison results are shown in Fig. 11. It can be seen from Fig. 11(a) that the phase-variable profile from the present model agrees well with the initial profile; While for the YG-LBE model, the phase variable of the small droplet deviates from the initial one greatly. This deviation results from the numerical dissipation of small droplet whose mass diffuses into the surrounding gas phase, increasing the mass of the surrounding fluid. Figure 11(b) reveals that the transport flux induced by the chemical potential gradient obtained by the present model is close to a constant value with the magnitude of 10^{-9} ; While for the

YG-LBE model, the transport flux fluctuates significantly in the region between the two droplets.

The time history of the mass ratio between the small and large droplets is shown in Fig. 12. It is clear that with the increase of time, the mass ratio predicted by the YG-LBE model decreases until it reaches zero. On the other hand, the mass ratio predicted by the present model decreases at the initial stage and then remains constant during the whole simulation process. The above results show that the present model provides lower numerical dissipation and better numerical resolution in simulating immiscible droplets than the YG-LBE model does.

E. Falling droplets

The process of two droplets falling under gravity is simulated in this section. The computational domain is $[0, L_0] \times [0, 3L_0]$. Initially, the smaller droplet of radius R_1 is placed at the location of $(L_0/2, 3L_0 - 2R_1)$, and the bigger droplet of radius R_2 is placed at the location of $(L_0/2, 3L_0 - 14R_1)$. The no-slip boundary condition is

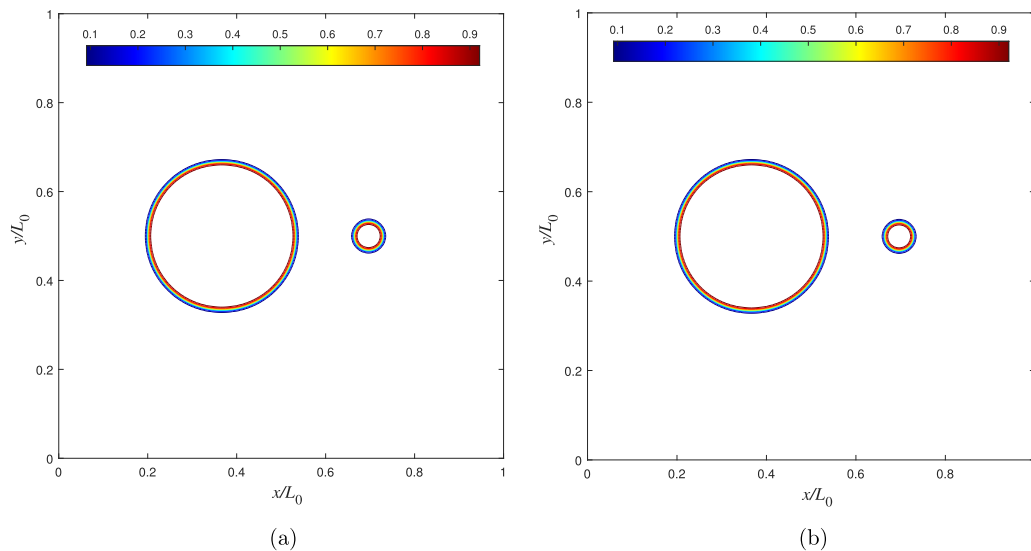


FIG. 10. The snapshots of two static droplets at different time obtained by the present model. (a) $T_r = 2000$, (b) $T_r = 3200$.

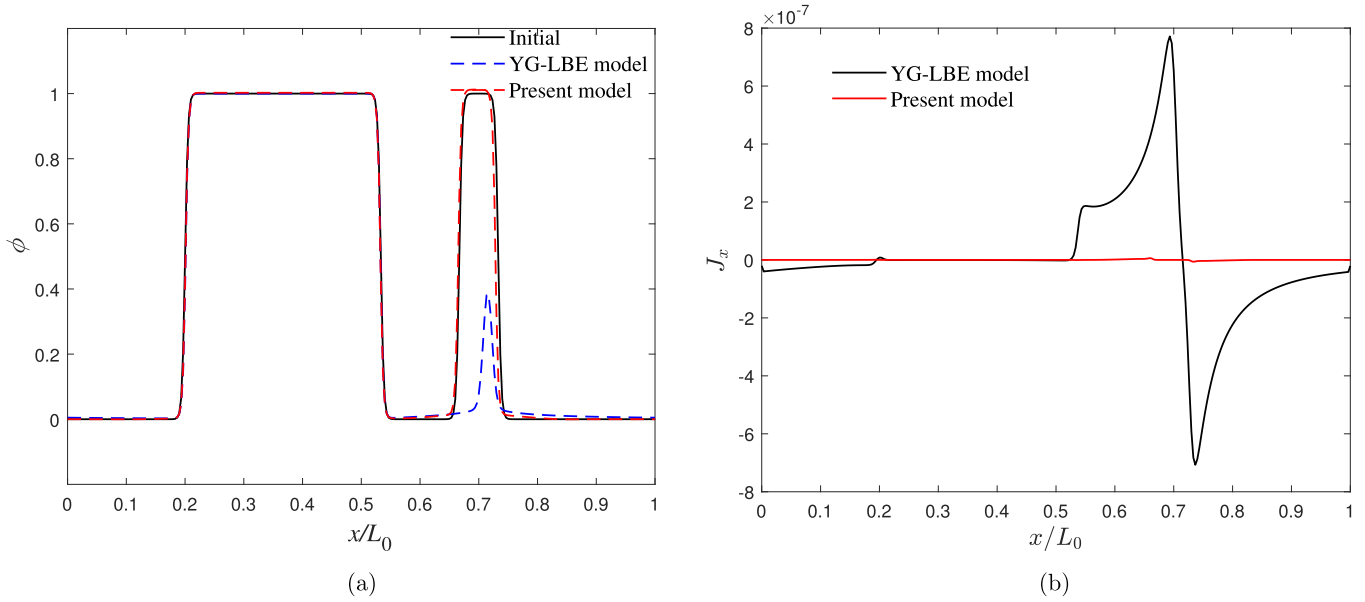


FIG. 11. The phase variable (a) and transport flux (b) profiles across the droplet center at $T_r = 2800$.

applied to the top and bottom walls, and period boundary condition is used for vertical boundaries. The dimensionless Eötvös number is defined as $Eo = 4g(\rho_l - \rho_g)R_2^2/\sigma$. In the simulations, we set: $Eo = 10$, $\rho_l = 3$, $\rho_g = 1$, $\mu_l = 0.075$, $\mu_g = 0.025$, $\sigma = 5 \times 10^{-4}$, $M_0 = 1$, $\tau_g = 0.8$, $L_0 = 160$, $R_1 = 8$, $R_2 = 40$, $B = 0$.

Figure 13 presents the interfacial evolution of the falling droplets under gravity. It can be seen that the shapes and positions of the large droplet predicted by the two models are almost identical. However, the size of the small droplet predicted by the YG-LBE model gradually decreases with the evolution of time, while the present model still maintains the size of small droplet well during the falling process. To confirm this point, we further increase the radius of the small droplet to 24 and simulate the same case in Fig. 13. Figure 14 presents the interfacial evolution of the falling droplets at

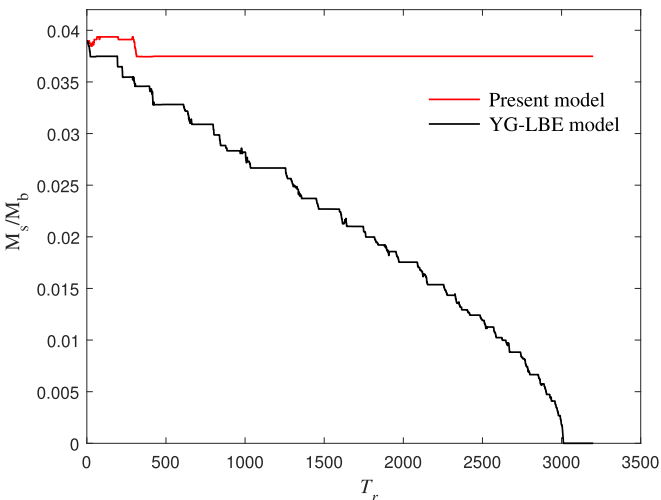


FIG. 12. Time history of the mass ratio of the small droplet to the large droplet.

$R_2/R_1 = 5/3$. It can be observed that both shapes and positions of the droplets predicted by the two models have little difference. The falling droplets tests demonstrate the capacity of the present model to reduce the numerical dissipation of small droplet and to accurately describe the dynamic behavior of small droplet.

In order to demonstrate the effect of the free parameter B on improving the proposed model's ability to handle a large viscosity ratio problem, the process of droplets falling at different viscosity ratio ($\mu_r = \mu_l/\mu_g$) is investigated. In the simulations, we set: $Eo = 10$, $\rho_l = 3$, $\rho_g = 1$, $\mu_g = 0.005$, $\sigma = 5 \times 10^{-4}$, $M_0 = 0.2$, $\tau_g = 0.8$, $L_0 = 160$, $R_1 = 24$, $R_2 = 40$. Firstly, the performances of the present model for $B = 0$ and $B \neq 0$ are compared. For $B \neq 0$, we take $\tau_f = 0.9$, and the value of parameter B can be calculated by Eq. (17). The velocity and pressure structure along x direction at $\mu_r = 10$ and $t = 100$ are shown in Fig 15. It can be seen that for $B = 0$ the velocity and pressure fields oscillate dramatically, and the model becomes unstable. While for $B \neq 0$, both the velocity and pressure fields vary smoothly, which indicates that the presence of parameter B improves the numerical stability of the model. Figure 16 further shows the interfacial evolution of the falling droplets obtained from the present model ($B \neq 0$) for different viscosity ratios. It can be seen that at small viscosity ratio, the topological structure of the droplets changes dramatically. However, with the increase of the viscosity ratio the droplet remains almost circular during the falling process until contact occurs, and the time for the droplets to begin contacting becomes longer. The above results confirm the capability of the present model in handling two-phase flows with large viscosity ratio.

F. Phase separation of binary fluid

To further verify the performance of the present model in handling two-phase flows, the phase separation of binary fluid [18,50] was investigated. The initial phase-variable

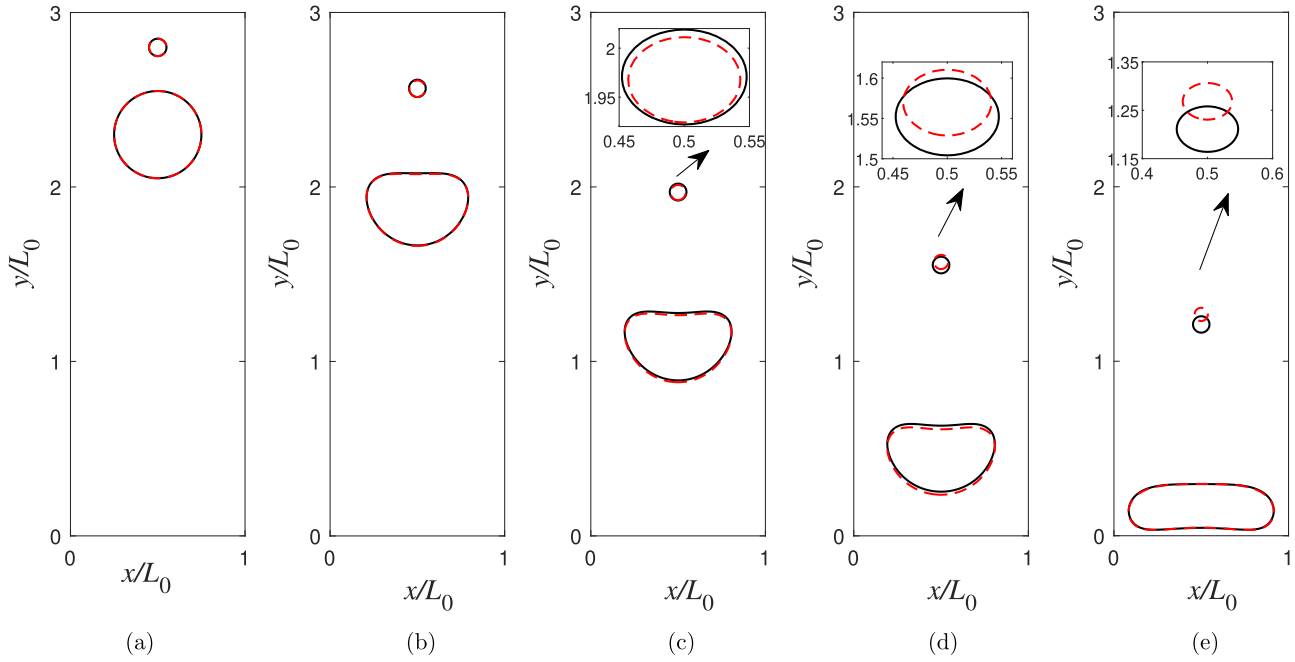


FIG. 13. Interfacial evolution of falling droplets at $R_2/R_1 = 5$. The solid and dashed lines are the results obtained by the present and YG-LBE models, respectively. (a) $t = 0$, (b) $t = 4.0 \times 10^4$, (c) $t = 1.0 \times 10^5$, (d) $t = 1.5 \times 10^5$, (e) $t = 2.0 \times 10^5$.

distribution with small fluctuations can be given by

$$\phi(x, y) = \phi_0 + \text{rand}(x, y), \quad (27)$$

where $\text{rand}(x, y)$ is a random function with a maximum amplitude of 0.01. ϕ_0 is the initial mean phase variable, and we take $\phi_0 = 1/3$ where the spinodal decomposition occurs. Then the initial compositional fluctuations will be imposed on a homogeneous mixture. The computational domain is set to $L_x \times L_y = 200 \times 200$ with periodic boundary condi-

tions applied to all boundaries. The numerical parameters are fixed as $\rho_l = 2, \rho_g = 1, \mu_l = 0.2, \mu_g = 0.0001, W = 4, \sigma = 0.002, M_0 = 0.1$. In the present model, we fix $\tau_f = \tau_g = 0.8$, and the values of parameters A, B can be obtained by Eqs. (15) and (21).

Figure 17 shows the distribution of velocity obtained from the two models at $t/t_v=750$ with $t_v = \mu_l W/\sigma$ being the viscous time of liquid phase. It can be seen that for the YG-LBE model the velocity field generates high-frequency

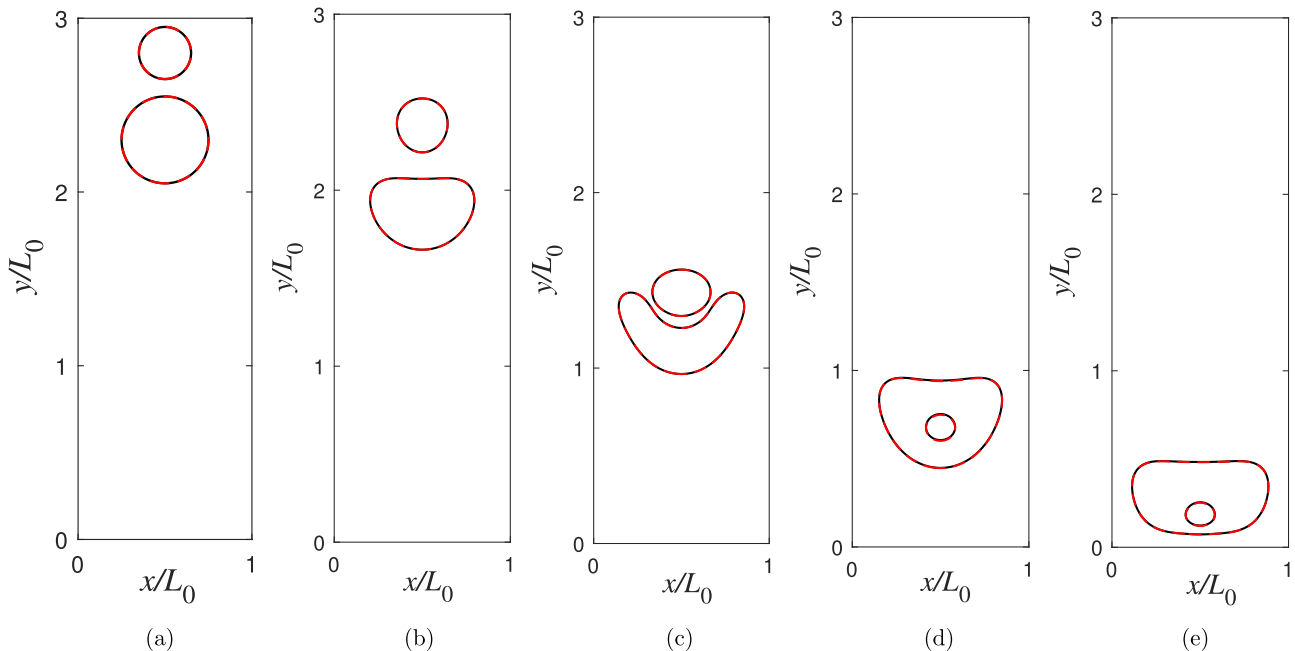


FIG. 14. Interfacial evolution of falling droplets at $R_2/R_1 = 5/3$. The solid and dashed lines are the results obtained by the present and YG-LBE models, respectively. (a) $t = 0$, (b) $t = 4.0 \times 10^4$, (c) $t = 1.0 \times 10^5$, (d) $t = 1.5 \times 10^5$, (e) $t = 2.0 \times 10^5$.

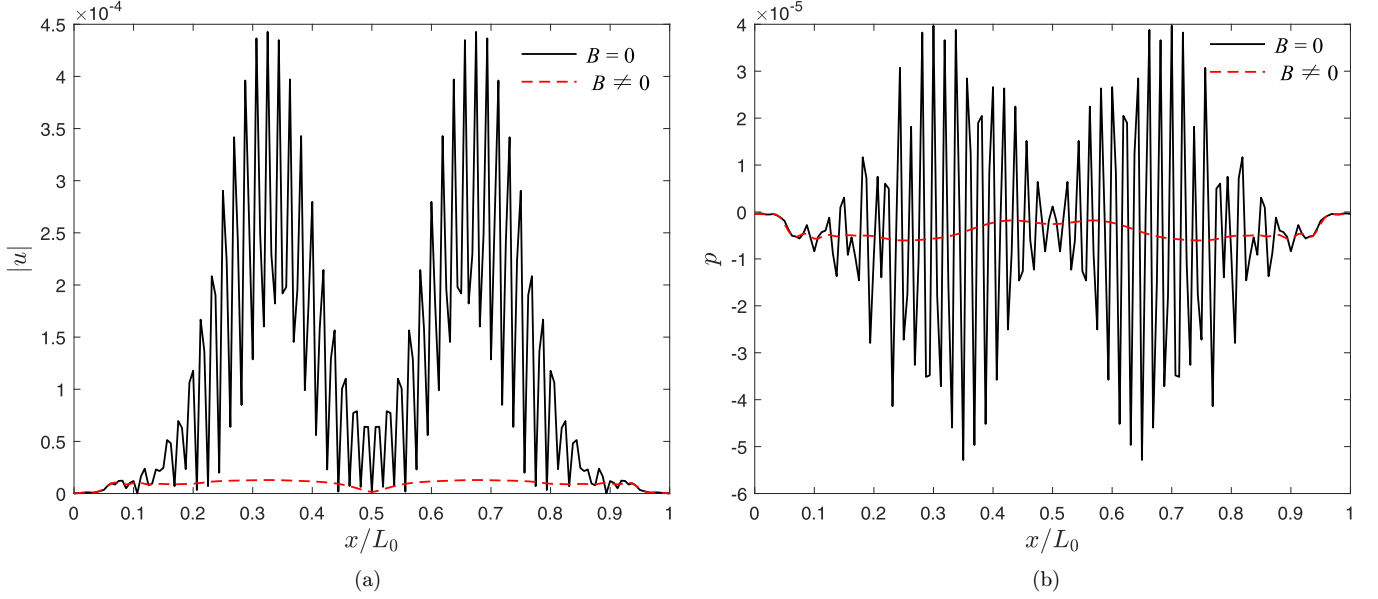


FIG. 15. The distribution of velocity (a) and pressure (b) for different B values at $\mu_r = 10$ and $t = 100$.

oscillations and numerical instability occurs, resulting in subsequent procedure divergence; However, for the present model the high-frequency oscillations in the velocity field are significantly suppressed. Figure 18 shows the time evolution of the phase-variable distribution during the phase separating process obtained from the present model. It can be found that the fluctuation of the initial phase variable leads to an inhomogeneous spatial distribution, followed by the generation of a series of small droplets. These small droplets gradually become larger under the action of flow and surface tension, and eventually lead to phase separation. Further increasing the viscosity ratio to 10^4 , the present model still accurately

describes the phase separation process. The phase separation of binary fluid problem indicates that the present model can improve the numerical stability at large viscosity ratio.

V. CONCLUSION

In this paper, we proposed an improved LBE model for quasi-incompressible two-phase flows, which overcomes the difficulty that the original LBE model cannot handle variable mobility in the singular CHE. The Chapman-Enskog analysis indicated that the proposed model could recover the CHE correctly. A series of numerical tests were conducted to verify

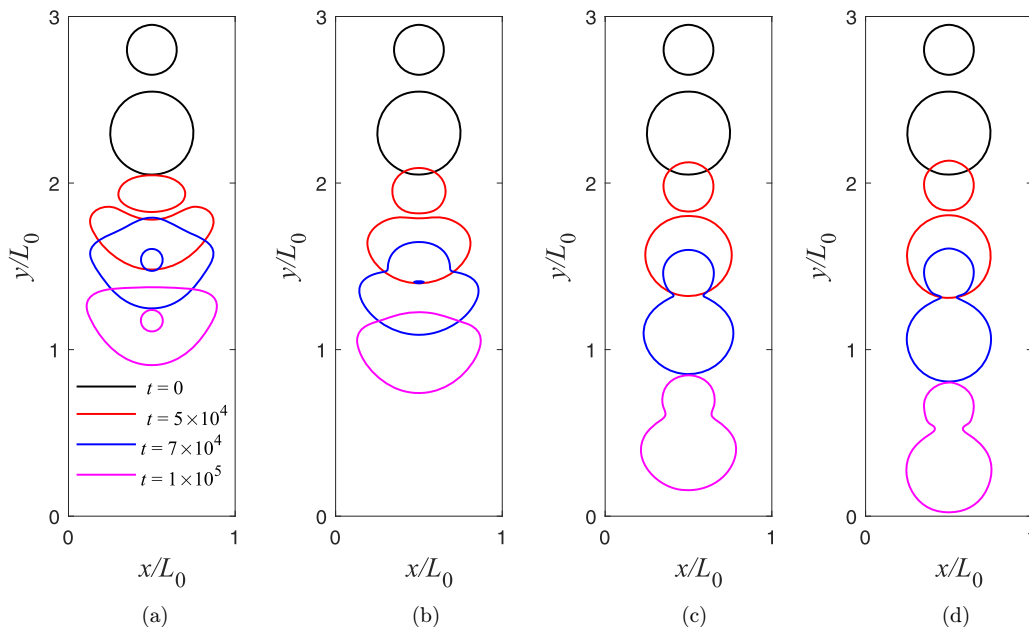


FIG. 16. Interfacial evolution of falling droplets obtained from the present model for different viscosity ratio. (a) $\mu_r = 10$, (b) $\mu_r = 10^2$, (c) $\mu_r = 10^3$, (d) $\mu_r = 10^4$.

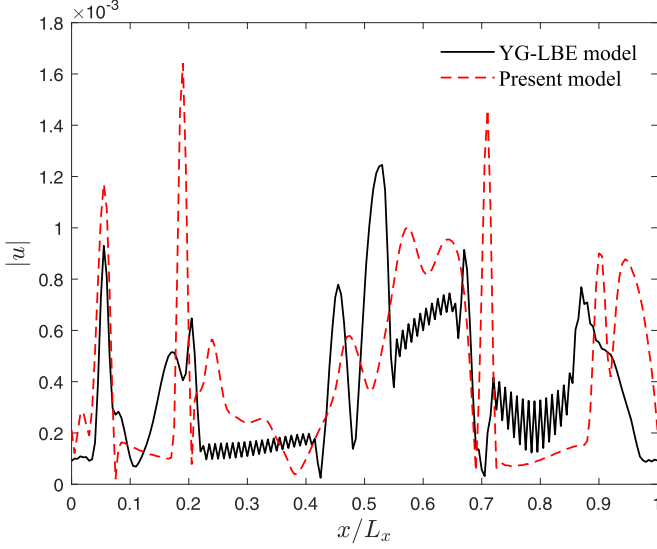


FIG. 17. The distribution of velocity along $y/L_y = 0.5$ for the phase separation problem at $t/t_v = 750$.

the accuracy of the proposed model to capture the phase interface.

In the interface-tracking tests, the results of benchmark tests showed that the proposed model could capture the phase interface with improved accuracy and stability compared with the YG-LBE model, in particular at high Peclet number. In the two-phase flow tests, the proposed model was coupled with LBE model for the hydrodynamic equations, the undesired phenomenon of spontaneous droplet disappearance in phase-field simulations was effectively suppressed. The tests of double-stationary droplets and droplets falling indicated that the proposed LBE model tended to maintain the size and position of the small droplet better and showed lower numerical dissipation than the original LBE model. Moreover, the results of droplets falling and phase separation of binary fluid problems indicated that the present model is capable of handling two-phase flows with large viscosity ratio up to the magnitude of 10^4 .

ACKNOWLEDGMENTS

This study is financially supported by the National Natural Science Foundation of China (Grant No. 51836003), and the Interdisciplinary Research Program of HUST (Grant No. 2023JCYJ002). The computation is completed in the HPC Platform of Huazhong University of Science and Technology.

APPENDIX: CHAPMAN-ENSKOG ANALYSIS OF THE LBE MODEL FOR THE SINGULAR CHE

The macroscopic governing equation can be obtained by applying the Chapman-Enskog analysis to LBE [Eq. (9)]. Specifically, we introduce the following multiscale expansions:

$$g_i = g_i^{(0)} + \varepsilon g_i^{(1)} + \varepsilon^2 g_i^{(2)} + \dots, \quad R_i = \varepsilon R_i^{(0)}, \quad \partial_t = \varepsilon \partial_{t_0} + \varepsilon^2 \partial_{t_1}, \quad \nabla = \varepsilon \nabla_0, \quad g_i^{\text{eq}} = g_i^{(0)} + \varepsilon g_i^{(1)}, \quad (\text{A1})$$

where

$$g_i^{(0)} = H_i + \omega_i \phi s_i(\mathbf{u}), \quad g_i^{(1)} = \omega_i A \delta_t \alpha c_i \cdot \nabla \mu \phi. \quad (\text{A2})$$

The order moments of the equilibrium distribution function and the forcing term are given by

$$\sum_i g_i^{(0)} = \phi, \quad \sum_i c_i g_i^{(0)} = \phi \mathbf{u}, \quad \sum_i c_i c_i g_i^{(0)} = \phi \mathbf{u} \mathbf{u} + c_s^2 \mu, \quad \sum_i g_i^{(1)} = 0, \quad (\text{A3a})$$

$$\sum_i c_i g_i^{(1)} = A \delta_t \alpha c_s^2 \nabla_0 \mu, \quad \sum_i R_i = 0, \quad \sum_i c_i R_i = \frac{\phi}{\rho} \mathbf{G}, \quad (\text{A3b})$$

where $\mathbf{G} = \varepsilon \mathbf{G}^0 = -\nabla p + \mathbf{F}$. With the help of Eqs. (A1) and (A3), the following equations can be obtained:

$$\sum_i g_i^{(k)} = 0, \quad (k \geq 1), \quad \sum_i R_i^{(0)} = 0, \quad \sum_i c_i R_i^{(0)} = \frac{\phi}{\rho} \mathbf{G}^0. \quad (\text{A4})$$

Applying Taylor expansion for Eq. (9), one can obtain

$$D_i g_i + \frac{\delta_t}{2} D_i^2 g_i = -\frac{1}{\tau_g \delta_t} [g_i(\mathbf{x}, t) - g_i^{\text{eq}}(\mathbf{x}, t)] + \left(1 - \frac{1}{2\tau_g}\right) R_i(\mathbf{x}, t). \quad (\text{A5})$$

Substituting Eq. (A1) into Eq. (A5), the multiscale equations can be obtained:

$$\varepsilon^0: \quad g_i^{(0)} = g_i^{\text{eq}}, \quad (\text{A6a})$$

$$\varepsilon^1: \quad D_{0i} g_i^{(0)} = -\frac{1}{\tau_g \delta_t} (g_i^{(1)} - g_i^{\text{eq}(1)}) + \left(1 - \frac{1}{2\tau_g}\right) R_i^{(0)}, \quad (\text{A6b})$$

$$\varepsilon^2: \quad \partial_{t_1} g_i^{(0)} + D_{0i} \left(1 - \frac{1}{2\tau_g}\right) g_i^{(1)} + \frac{\delta_t}{2} D_{0i} \left(1 - \frac{1}{2\tau_g}\right) R_i^{(0)} + D_{0i} \frac{1}{2\tau_g} g_i^{\text{eq}(1)} = -\frac{1}{\delta_t \tau_g} g_i^{\text{eq}(2)}. \quad (\text{A6c})$$

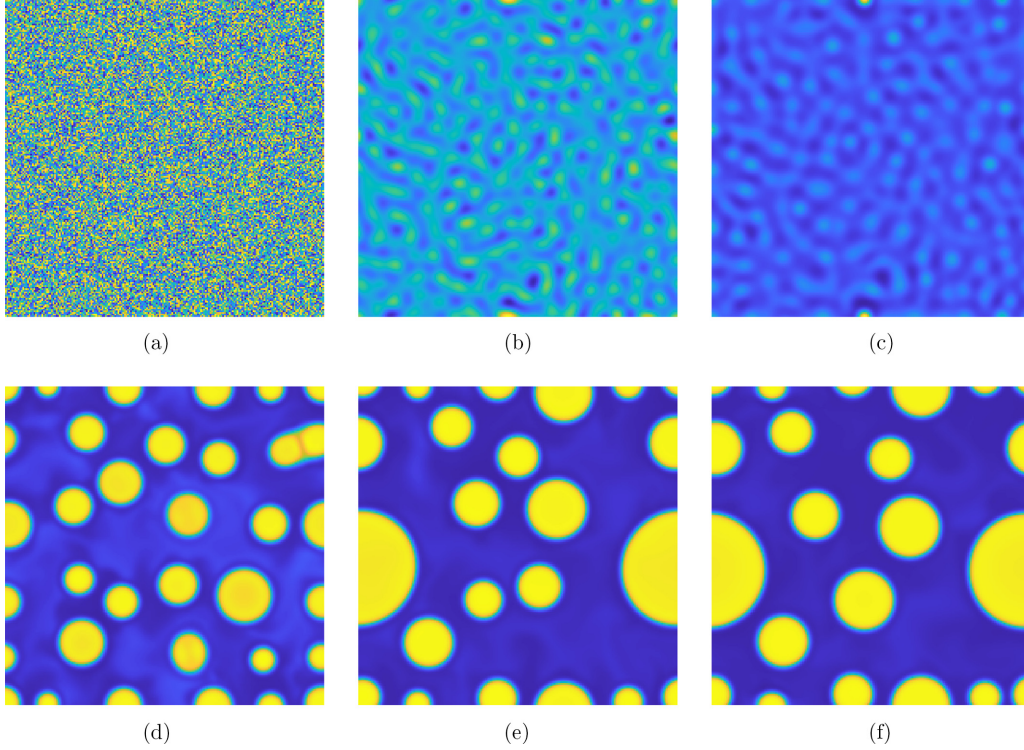


FIG. 18. Time evolution of the phase-variable distribution during the phase separating process. (a) $t_v = 0$, (b) $t_v = 125$, (c) $t_v = 250$, (d) $t_v = 500$, (e) $t_v = 750$, (f) $t_v = 1000$.

Taking the zero-order moment of Eqs. (A6b) and (A6c), respectively, we can obtain

$$\partial_{t_0}\phi + \nabla_0 \cdot (\phi \mathbf{u}) = 0, \quad (\text{A7})$$

$$\partial_{t_1}\phi + \left(1 - \frac{1}{2\tau_g}\right) \nabla_0 \cdot \left(\sum_i c_i g_i^{(1)}\right) + \frac{\delta_t}{2} \left(1 - \frac{1}{2\tau_g}\right) \nabla_0 \cdot \left(\frac{\phi}{\rho} \mathbf{G}^{(0)}\right) + \frac{1}{2\tau_g} \nabla_0 \cdot (A \delta_t \alpha c_s^2 \nabla_0 \mu) = 0. \quad (\text{A8})$$

The term of $\sum_i c_i g_i^{(1)}$ in Eq. (A8) can be obtained from Eq. (A6b):

$$\begin{aligned} \sum_i c_i g_i^{(1)} &= -\delta_t \tau_g \partial_{t_0}(\phi \mathbf{u}) - \delta_t \tau_g \nabla_0 \cdot (\phi \mathbf{u} \mathbf{u} + c_s^2 \mu) + \left(\tau_g - \frac{1}{2}\right) \delta_t \frac{\phi}{\rho} \mathbf{G}^{(0)} + A \delta_t \alpha c_s^2 \nabla_0 \mu \\ &= (A - \tau_g) \delta_t \alpha c_s^2 \nabla_0 \mu - \frac{1}{2} \delta_t \frac{\phi}{\rho} \mathbf{G}^{(0)}. \end{aligned} \quad (\text{A9})$$

Substituting Eq. (A9) into Eq. (A8), Eq. (A8) can be rewritten as

$$\partial_{t_1}\phi = \nabla_0 \cdot (M_\phi \nabla_0 \mu_\phi), \quad (\text{A10})$$

where $M_\phi = c_s^2 \delta_t \alpha (\tau_g - \frac{1}{2} - A)$ is the mobility. Combining Eqs. (A7) and (A10), the CHE can be correctly recovered by the present model

$$\partial_t \phi + \nabla \cdot (\phi \mathbf{u}) = \nabla \cdot (M_\phi \nabla \mu_\phi). \quad (\text{A11})$$

Considering $\varepsilon g_i^{(1)} = g_i - g_i^{e(0)}$, multiplying ε on both sides of Eq. (A9), we can obtain

$$\nabla \mu = \frac{\sum_i c_i (g_i - g_i^{e(0)}) - \frac{1}{2} \delta_t \frac{\phi}{\rho} \nabla P}{(A - \tau_g) \delta_t \alpha c_s^2 + \frac{1}{2} \delta_t \frac{\phi^2}{\rho}}. \quad (\text{A12})$$

[1] C. W. Hirt and B. D. Nichols, Volume of fluid (VOF) method for the dynamics of free boundaries, *J. Comput. Phys.* **39**, 201 (1981).

[2] J. A. Sethian, Level set methods: Evolving interfaces in geometry, fluid mechanics, computer vision, and materials science, Cambridge Monogr. Appl. Comput. Math. **3** (1996).

- [3] S. O. Unverdi and G. Tryggvason, A front-tracking method for viscous, incompressible, multi-fluid flows, *J. Comput. Phys.* **100**, 25 (1992).
- [4] K. Xu, A kinetic method for hyperbolic–elliptic equations and its application in two-phase flow, *J. Comput. Phys.* **166**, 383 (2001).
- [5] Q. Li, K. H. Luo, Q. Kang, Y. He, Q. Chen, and Q. Liu, Lattice Boltzmann methods for multiphase flow and phase-change heat transfer, *Prog. Energy Combust. Sci.* **52**, 62 (2016).
- [6] Z. Guo and K. Xu, Progress of discrete unified gas-kinetic scheme for multiscale flows, *Adv. Aerodyn.* **3**, 6 (2021).
- [7] Z. Guo and C. Shu, *Lattice Boltzmann Method and its Applications in Engineering* (World Scientific, Singapore, 2013).
- [8] H. Huang, M. Sukop, and X. Lu, *Multiphase Lattice Boltzmann Methods: Theory and Application* (John Wiley & Sons, Hoboken, New Jersey, 2015).
- [9] A. K. Gunstensen, D. H. Rothman, S. Zaleski, and G. Zanetti, Lattice Boltzmann model of immiscible fluids, *Phys. Rev. A* **43**, 4320 (1991).
- [10] M. Latva-Kokko and D. H. Rothman, Diffusion properties of gradient-based lattice Boltzmann models of immiscible fluids, *Phys. Rev. E* **71**, 056702 (2005).
- [11] X. Shan and H. Chen, Lattice Boltzmann model for simulating flows with multiple phases and components, *Phys. Rev. E* **47**, 1815 (1993).
- [12] X. Shan and G. Doolen, Multicomponent lattice-Boltzmann model with interparticle interaction, *J. Stat. Phys.* **81**, 379 (1995).
- [13] M. R. Swift, W. R. Osborn, and J. M. Yeomans, Lattice Boltzmann simulation of nonideal fluids, *Phys. Rev. Lett.* **75**, 830 (1995).
- [14] M. R. Swift, E. Orlandini, W. R. Osborn, and J. M. Yeomans, Lattice Boltzmann simulations of liquid-gas and binary fluid systems, *Phys. Rev. E* **54**, 5041 (1996).
- [15] X. He, S. Chen, and R. Zhang, A lattice Boltzmann scheme for incompressible multiphase flow and its application in simulation of Rayleigh-Taylor instability, *J. Comput. Phys.* **152**, 642 (1999).
- [16] H. Liang, B. C. Shi, Z. H. Guo, and Z. Chai, Phase-field-based multiple-relaxation-time lattice Boltzmann model for incompressible multiphase flows, *Phys. Rev. E* **89**, 053320 (2014).
- [17] M. R. Moldover and J. W. Cahn, An interface phase transition: complete to partial wetting, *Science* **207**, 1073 (1980).
- [18] H. Liang, J. Xu, J. Chen, H. Wang, Z. Chai, and B. Shi, Phase-field-based lattice Boltzmann modeling of large-density-ratio two-phase flows, *Phys. Rev. E* **97**, 033309 (2018).
- [19] Y. Q. Zu and S. He, Phase-field-based lattice Boltzmann model for incompressible binary fluid systems with density and viscosity contrasts, *Phys. Rev. E* **87**, 043301 (2013).
- [20] T. Lee and L. Liu, Lattice Boltzmann simulations of micron-scale drop impact on dry surfaces, *J. Comput. Phys.* **229**, 8045 (2010).
- [21] J. W. Cahn and J. E. Hilliard, Free energy of a nonuniform system. I. interfacial free energy, *J. Chem. Phys.* **28**, 258 (1958).
- [22] J. W. Cahn and J. E. Hilliard, Free energy of a nonuniform system. III. nucleation in a two-component incompressible fluid, *J. Chem. Phys.* **31**, 688 (1959).
- [23] S. M. Allen and J. W. Cahn, A microscopic theory for antiphase boundary motion and its application to antiphase domain coarsening, *Acta Metall.* **27**, 1085 (1979).
- [24] Y. Sun and C. Beckermann, Sharp interface tracking using the phase-field equation, *J. Comput. Phys.* **220**, 626 (2007).
- [25] A. Tiribocchi, N. Stella, G. Gonnella, and A. Lamura, Hybrid lattice Boltzmann model for binary fluid mixtures, *Phys. Rev. E* **80**, 026701 (2009).
- [26] J. Huang, C. Shu, J. Feng, and Y. Chew, A phase-field-based hybrid lattice-Boltzmann finite-volume method and its application to simulate droplet motion under electrowetting control, *J. Adhes. Sci. Technol.* **26**, 1825 (2012).
- [27] J.-J. Huang, H. Huang, C. Shu, Y. T. Chew, and S.-L. Wang, Hybrid multiple-relaxation-time lattice-Boltzmann finite-difference method for axisymmetric multiphase flows, *J. Phys. A: Math. Theor.* **46**, 055501 (2013).
- [28] J. Shao and C. Shu, A hybrid phase field multiple relaxation time lattice Boltzmann method for the incompressible multiphase flow with large density contrast, *Int. J. Numer. Methods Fluids* **77**, 526 (2015).
- [29] H. Zheng, C. Shu, and Y.-T. Chew, A lattice Boltzmann model for multiphase flows with large density ratio, *J. Comput. Phys.* **218**, 353 (2006).
- [30] C. Zhang, Z. Guo, and H. Liang, High-order lattice-Boltzmann model for the Cahn-Hilliard equation, *Phys. Rev. E* **99**, 043310 (2019).
- [31] J. Shen, X. Yang, and Q. Wang, Mass and volume conservation in phase field models for binary fluids, *Commun. Comput. Phys.* **13**, 1045 (2013).
- [32] K. Yang and Z. Guo, Lattice Boltzmann method for binary fluids based on mass-conserving quasi-incompressible phase-field theory, *Phys. Rev. E* **93**, 043303 (2016).
- [33] T. Zhang and Q. Wang, Cahn-Hilliard vs singular Cahn-Hilliard equations in phase field modeling, *Commun. Comput. Phys.* **7**, 362 (2010).
- [34] R. B. Bird, R. C. Armstrong, and O. Hassager, *Dynamics of Polymeric Liquids*. Vol. 1: Fluid Mechanics, 1987.
- [35] M. Doi, S. F. Edwards, and S. F. Edwards, *The Theory of Polymer Dynamics* (Oxford University Press, 1988), Vol. 73.
- [36] J. Kim, A numerical method for the Cahn-Hilliard equation with a variable mobility, *Commun. Nonlinear Sci. Numer. Simul.* **12**, 1560 (2007).
- [37] J. Langer, M. Bar-On, and H. D. Miller, New computational method in the theory of spinodal decomposition, *Phys. Rev. A* **11**, 1417 (1975).
- [38] J. K. Wolterink, G. T. Barkema, and S. Puri, Spinodal decomposition via surface diffusion in polymer mixtures, *Phys. Rev. E* **74**, 011804 (2006).
- [39] F. Boyer and C. Lapuerta, Study of a three component Cahn-Hilliard flow model, *ESAIM: Math. Modell. Numer. Anal.* **40**, 653 (2006).
- [40] C. Zhang, Z. Guo, and L.-P. Wang, Improved well-balanced free-energy lattice Boltzmann model for two-phase flow with high Reynolds number and large viscosity ratio, *Phys. Fluids* **34**, 012110 (2022).
- [41] X. Meng and Z. Guo, Multiple-relaxation-time lattice Boltzmann model for incompressible miscible flow with large viscosity ratio and high Péclet number, *Phys. Rev. E* **92**, 043305 (2015).
- [42] T. Inamuro, A lattice kinetic scheme for incompressible viscous flows with heat transfer, *Philos. Trans. R. Soc. London A* **360**, 477 (2002).

- [43] D. Jacqmin, Calculation of two-phase Navier-Stokes flows using phase-field modeling, *J. Comput. Phys.* **155**, 96 (1999).
- [44] Y. Yan and Y. Zu, A lattice Boltzmann method for incompressible two-phase flows on partial wetting surface with large density ratio, *J. Comput. Phys.* **227**, 763 (2007).
- [45] J. W. Cahn and J. E. Taylor, Overview no. 113 surface motion by surface diffusion, *Acta Metall. Mater.* **42**, 1045 (1994).
- [46] Q. Lou, Z. Guo, and B. Shi, Effects of force discretization on mass conservation in lattice Boltzmann equation for two-phase flows, *Europhys. Lett.* **99**, 64005 (2012).
- [47] H. Liang, Z. H. Chai, B. C. Shi, Z. L. Guo, and T. Zhang, Phase-field-based lattice Boltzmann model for axisymmetric multiphase flows, *Phys. Rev. E* **90**, 063311 (2014).
- [48] S. T. Zalesak, Fully multidimensional flux-corrected transport algorithms for fluids, *J. Comput. Phys.* **31**, 335 (1979).
- [49] C. Liu and J. Shen, A phase field model for the mixture of two incompressible fluids and its approximation by a Fourier-spectral method, *Physica D: Nonlin. Phenom.* **179**, 211 (2003).
- [50] J. W. Cahn, Phase separation by spinodal decomposition in isotropic systems, *J. Chem. Phys.* **42**, 93 (1965).